

Article

Novel Co-Cu-Based Immiscible Medium-Entropy Alloys with Promising Mechanical Properties

Sujung Son ¹, Jongun Moon ^{1,*}, Hyeonseok Kwon ¹, Peyman Asghari Rad ¹, Hidemi Kato ² and Hyoung Seop Kim ^{1,2,3,*} 

¹ Department of Materials Science and Engineering, Pohang University of Science and Technology (POSTECH), Pohang 37673, Korea; sjson@postech.ac.kr (S.S.); hyunsug007@postech.ac.kr (H.K.); asghari90@postech.ac.kr (P.A.R.)

² Institute for Materials Research, Tohoku University, Sendai 980-8577, Japan; hikato@imr.tohoku.ac.jp

³ Graduate Institute for Ferrous Technology, Pohang University of Science and Technology (POSTECH), Pohang 37673, Korea

* Correspondence: moonj6513@postech.ac.kr (J.M.); hskim@postech.ac.kr (H.S.K.); Tel.: +82-54-279-5413 (J.M.); +82-54-279-2150 (H.S.K.); Fax: +82-54-279-3150 (J.M. & H.S.K.)

Abstract: New $\text{Al}_x\text{Co}_{50-x}\text{Cu}_{50-x}\text{Mn}_x$ ($x = 2.5, 10, \text{ and } 15$ atomic %, at%) immiscible medium-entropy alloys (IMMEAs) were designed based on the cobalt-copper binary system. Aluminum, a strong B2 phase former, was added to enhance yield strength and ultimate tensile strength, while manganese was added for additional solid solution strengthening. In this work, the microstructural evolution and mechanical properties of the designed Al-Co-Cu-Mn system are examined. The alloys exhibit phase separation into dual face-centered cubic (FCC) phases due to the miscibility gap of the cobalt-copper binary system with the formation of CoAl-rich B2 phases. The hard B2 phases significantly contribute to the strength of the alloys, whereas the dual FCC phases contribute to elongation mitigating brittle fracture. Consequently, analysis of the Al-Co-Cu-Mn B2-strengthened IMMEAs suggest that the new alloy design methodology results in a good combination of strength and ductility.

Keywords: medium-entropy alloy; alloy design; multiphase; miscibility gap; mechanical properties



Citation: Son, S.; Moon, J.; Kwon, H.; Asghari Rad, P.; Kato, H.; Kim, H.S.

Novel Co-Cu-Based Immiscible Medium-Entropy Alloys with Promising Mechanical Properties.

Metals **2021**, *11*, 238. <https://doi.org/10.3390/met11020238>

Academic Editor: Sergey V. Zherebtsov

Received: 6 January 2021

Accepted: 22 January 2021

Published: 1 February 2021

Publisher's Note: MDPI stays neutral with regard to jurisdictional claims in published maps and institutional affiliations.



Copyright: © 2021 by the authors. Licensee MDPI, Basel, Switzerland. This article is an open access article distributed under the terms and conditions of the Creative Commons Attribution (CC BY) license (<https://creativecommons.org/licenses/by/4.0/>).

1. Introduction

High-entropy alloys (HEAs) and medium-entropy alloys (MEAs) are composed of multi-principal elements with equiatomic or near-equiatomic compositions [1]. According to the concept of HEAs, alloys can be categorized based on configurational entropy (ΔS_{conf}) as HEAs, MEAs, and low-entropy alloys (LEAs), as follows [2]:

$$1.5R \leq \Delta S_{conf} \text{ (HEAs)}, \quad (1)$$

$$1.0R \leq \Delta S_{conf} \leq 1.5R \text{ (MEAs)}, \quad (2)$$

$$\Delta S_{conf} \leq 1.0R \text{ (LEAs)}, \quad (3)$$

where R is a gas constant. Over the past two decades, HEAs and MEAs have been attracting huge attention because of their potential to design numerous alloy systems [3] and their superior properties, e.g., high strength induced by solid solution strengthening [4,5], excellent fracture toughness at a cryogenic temperature [6], and irradiation resistance [7].

Furthermore, it is interesting to note that there are countless undiscovered HEAs and MEAs due to their high degree of freedom in alloy design. The initial concept of HEAs is defined as a single phase with equiatomic or near-equiatomic compositions [1]. However, the range of alloy design in HEA/MEAs has been expanded to non-equiatomic and/or multiphase alloys [8–21]. Recently developed ferrous MEAs are representative types of non-equiatomic MEAs [8], which utilize phase metastability, resulting in transformation-induced plasticity. Meanwhile, the design of multiphase HEAs/MEAs to enhance yield

strength (YS) is widely adopted through precipitation [9–14], martensitic transformation [10,15,16], and eutectic reaction [17–21]. In particular, many research groups focus on heterogeneous HEAs developed by the formation of multiple domains using heterogeneities in composition [22,23], grain size [24,25], and crystal structure [17–19,26]. Huge plastic incompatibility between hard and soft domains in heterogeneous microstructure leads to hetero-deformation induced (HDI) strengthening [27], which offers additional work hardening in addition to conventional strengthening mechanisms [27–29].

Recently, Moon et al. suggested a new strategy for designing “immiscible MEAs (IMMEAs)” utilizing a miscibility gap in the Cu-Fe binary system [26]. The miscibility gap is originated from the positive enthalpy of mixing and induces phase separation during cooling in diverse binary systems, e.g., Cu-Fe, Cu-Co, Fe-Mg, Cu-Cr, and Cu-Pb binary systems [30]. As a representative of IMMEAs, $\text{Al}_x(\text{CuFeMn})_{100-x}$ ($x = 0, 7.5,$ and 15 at%) alloys show phase separation based on the immiscible nature of the Cu-Fe binary system. These alloys exhibit outstanding mechanical properties originated from synergetic strengthening of solid solution strengthening, HDI strengthening at phase boundaries, and partially recrystallized microstructures. Notably, the design strategy of IMMEAs is expected to highly expand alloy design windows and, thus, the exploration of new immiscible alloy systems is promising.

In this work, we suggest novel Al-Co-Cu-Mn MEAs based on a Co-Cu binary system utilizing the concept of IMMEAs. The Co-Cu binary system is selected because the Co-Cu binary system shows a broad miscibility gap through wide ranges of composition and temperature, as in the Cu-Fe binary system. Therefore, the $\text{Al}_x\text{Co}_{50-x}\text{Cu}_{50-x}\text{Mn}_x$ ($x = 2.5,$ $10,$ 15 at%) alloys were designed, referred to as the 2.5Al, 10Al, and 15Al alloys according to the atomic percent of Al. The microstructural evolution and mechanical properties of the alloys are comprehensively examined to demonstrate the concept of the IMMEA design.

2. Materials and Methods

Ingots of $\text{Al}_{2.5}\text{Co}_{47.5}\text{Cu}_{47.5}\text{Mn}_{2.5}$, $\text{Al}_{10}\text{Co}_{40}\text{Cu}_{40}\text{Mn}_{10}$, and $\text{Al}_{15}\text{Co}_{35}\text{Cu}_{35}\text{Mn}_{15}$ (at%) were cast using vacuum induction melting equipment (MC100V, Indutherm, Walzbachtal-Wossingen, Germany). The elements used for casting had a purity higher than 99.9%. The as-cast ingots were homogenized at 800°C for 12 h in an argon atmosphere, followed by water quenching. To escape the possible difference in microstructures with positions where the samples were obtained, all samples for microstructural analyses and mechanical testing were obtained from the center of the homogenized ingots.

The samples for microstructural analyses were mechanically polished using silicon carbide papers of 600, 800, and 1200 grits, and finished with polishing by diamond suspensions of 3 and $1\ \mu\text{m}$. The crystal structures of the constituent phases of the alloys were identified using X-ray diffraction (XRD; D/MAX-2500, Rigaku, Tokyo, Japan) with Cu $K\alpha$ radiation and a step size of $2^\circ/\text{min}$. The composition and distribution of phases were carefully investigated using a field emission-scanning electron microscopy (FE-SEM; JSM-7100F; JEOL, Tokyo, Japan and XL30S FEG; Philips, Eindhoven, The Netherlands) equipped with back-scattered electron (BSE) and energy dispersive spectroscopy (EDS) detectors. The fraction of the constituent phases was evaluated using an image analyzer software (ImageJ software, National Institutes of Health, New York, NY, USA) at least three times for reliability. Electron backscatter diffraction (EBSD) analysis was conducted with a TSL EBSD system and interpreted with orientation imaging microscopy (OIM) collection software (TSL OIM Analysis 7, EDAX, Mahwah, NJ, USA).

Tensile tests were conducted using a universal testing machine (Instron 1361, Instron Co., Norwood, MA, USA) at room temperature. A precise engineering strain was obtained using the digital image correlation system (ARAMIS 12M; GOM, Braunschweig, Germany). The dimensions of dog-bone shaped samples were a gauge length of 1.5 mm, a width of 1.0 mm, and a thickness of 0.9 mm. Tensile tests were conducted at a quasi-static strain rate of $10^{-3}\ \text{s}^{-1}$ and were repeated at least three times for reproducibility. Loading-unloading-reloading (LUR) tests were performed using Instron1361. The same sample dimensions

and strain rate as the tensile tests were used for the LUR test. During the LUR tests, loading and unloading were repeated during deformation.

After the tensile tests, the fracture surfaces and longitudinal sections of the fractured samples were investigated using FE-SEM to understand the fracture mechanisms.

Thermo-Calc software and its upgraded version with thermodynamic database TCFE2000 were used to calculate the equilibrium phase diagrams from 400 to 1400 °C [31–33].

3. Results

3.1. Microstructures of the Al-Co-Cu-Mn IMMEAs

The design of the Al-Co-Cu-Mn alloys is targeting the B2-strengthened IMMEAs based on an immiscible Co-Cu binary system. As shown in the miscibility gap of the Co-Cu binary system in Figure 1a, Co and Cu have an immiscible nature, which divides Co-rich and Cu-rich phases over wide ranges of temperature and composition.

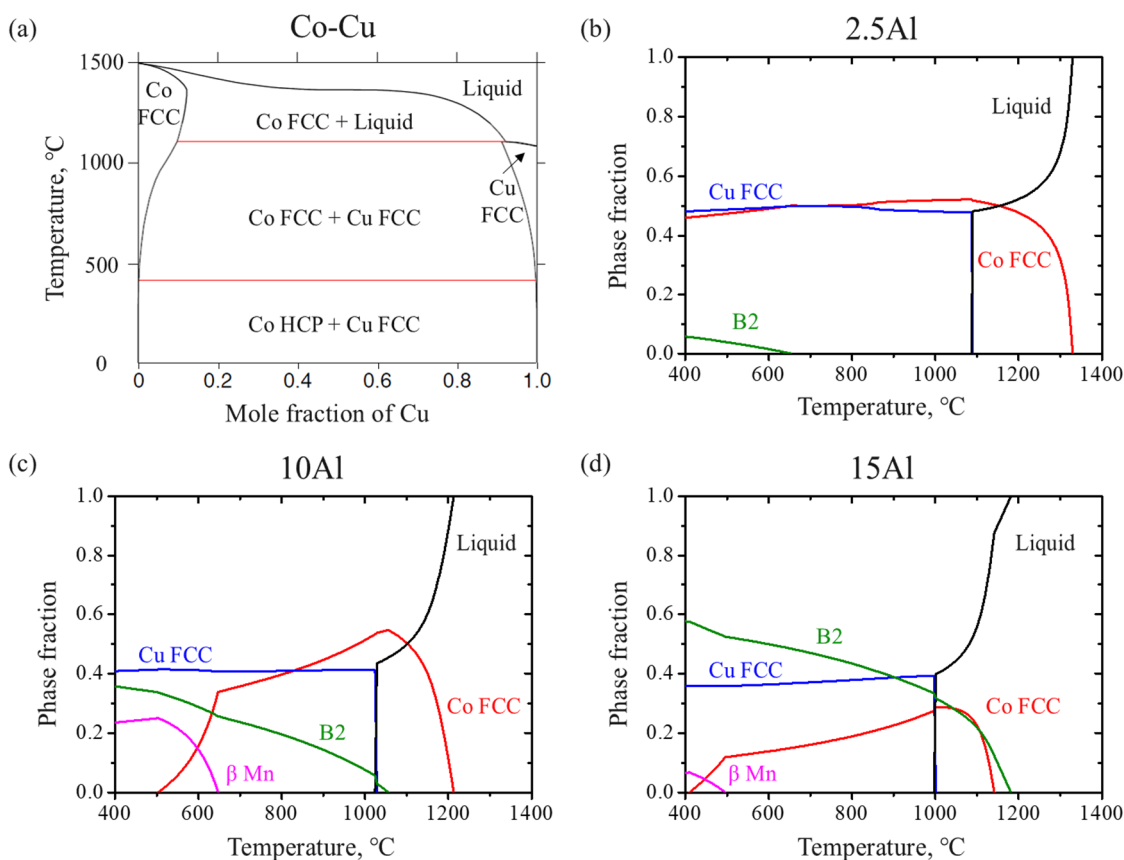


Figure 1. (a) Equilibrium phase diagram of Co-Cu binary system. Phase fraction as a function of temperature in the (b) 2.5Al, (c) 10Al, and (d) 15Al alloys.

For precipitation strengthening, aluminum as an alloying element was selected. Aluminum is a strong B2 former in Co-Al alloy [34] and changes the crystal structure of the Cu-rich phase from FCC to B2-ordered body-centered cubic (BCC) [35]. Manganese was selected as an alloying element for additional solid solution strengthening because of its broad range of solubility to Co- and Cu-matrix [36]. Based on the aforementioned concept, we designed the $\text{Al}_x\text{Co}_{50-x}\text{Cu}_{50-x}\text{Mn}_x$ ($x = 2.5, 10, 15$ at%) alloys to understand the microstructural evolution according to the contents of Al. Figure 1b–d are the calculated phase fraction versus temperature in the 2.5Al, 10Al, and 15Al alloys using the commercial program Thermo-Calc. As the contents of Al increases, the temperature range forming the B2 phase expands; thus, the phase fraction of the B2 phase is expected to increase. To

induce precipitation of the B2 phase to strengthen the alloys, we homogenized these alloys at 800 °C.

The XRD patterns of the homogenized 2.5Al, 10Al, and 15Al alloys are shown in Figure 2. The 2.5Al alloy with the smallest contents of Al and Mn exhibits dual FCC crystal structures, Co-rich FCC and Cu-rich FCC. In the 10Al and 15Al alloys, however, the peaks of the B2 phase appear as the Al and Mn contents increase. Therefore, the 10Al and 15Al alloys contain triple phases in their microstructure. According to the thermodynamic calculation (Figure 1b–d), the fraction of the B2 phase grows by consuming the fraction of Co-rich FCC because the present B2 phase is an Al-Co-ordered phase. Hence, the decline in the Co-rich FCC peaks is clearly observed in the XRD pattern of the 15Al alloy.

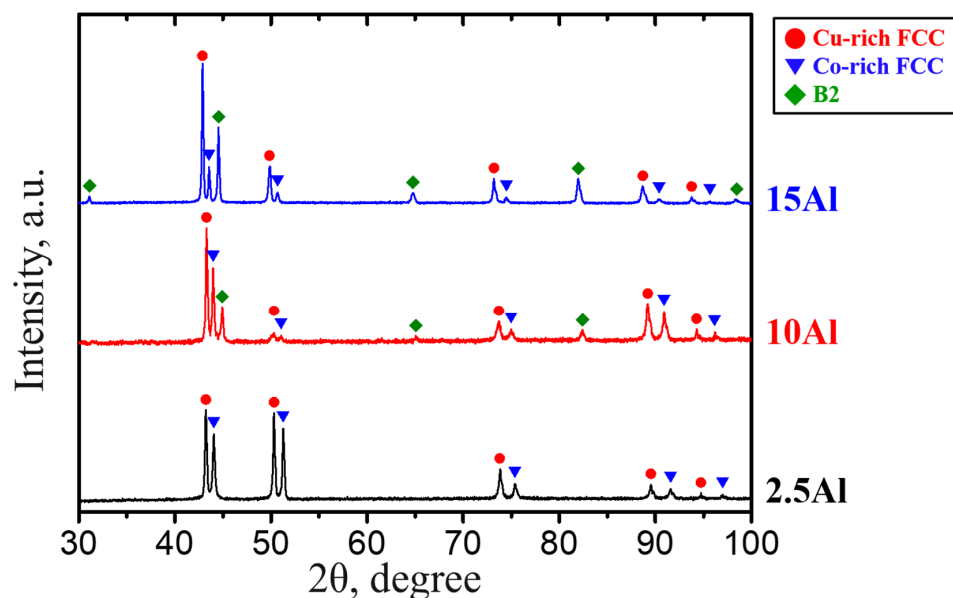


Figure 2. X-ray diffraction (XRD) patterns of the present alloys.

Figure 3 shows BSE images with EDS elemental maps for Al, Co, Cu, and Mn in the alloys. The dendritic Co-rich FCC and inter-dendritic Cu-rich FCC can be observed in Figure 3a. The Al and Mn are evenly distributed to dual FCC domains in the 2.5Al alloy. However, the B2 phases are formed in the 10Al and 15Al alloys, as shown in Figure 3b,c. It is noted that some nano-scale black dots, which are clarified as AlMn-rich oxide formed during casting, are also observed in the 2.5Al alloy (Figure 3d). Notably, the shape of the B2 phase is a needle-like precipitate in the 10Al alloy, while the dendritic microstructure of B2 is observed in the 15Al alloy. Most of the needle-shaped B2 precipitates in the 10Al alloy can be observed only inside the Cu-rich region (Figure 3b). From the EDS maps, the Al and Co are enriched in the B2 phase, indicating the B2 phase is Co-Al-ordered B2. Although the 15Al alloy contains a large amount of B2 phase, some Co-rich FCC phases remain, as shown in Figure 3c. The chemical composition and configurational entropy (ΔS_{mix}) of the constituent phases are given in Table 1. Mn contents in the Co-rich and Cu-rich domains increase with adding Mn into the alloys; however, the Al contents in the dual domains slightly decrease in the 15Al alloys accompanied by the formation of the B2 phase. Moreover, more Al and Mn are dissolved in the Co-rich FCC than in the Cu-rich FCC. The configurational entropy values of both Co-rich and Cu-rich FCC phases gradually increase with the addition of Al and Mn, leading to a mixture of the Co-rich medium-entropy phase (1.02R) and Cu-rich low-entropy phase (0.83R) in the 15Al alloy.

The fractions of the constituent phases evaluated by image analyzer software and thermodynamic calculation are given in Table 2. The phase fractions of the B2 phase were determined to be $15.33 \pm 0.47\%$ and $42.90 \pm 0.99\%$ in the 10Al and 15Al alloys, respectively, showing good consistency with thermodynamic calculations.

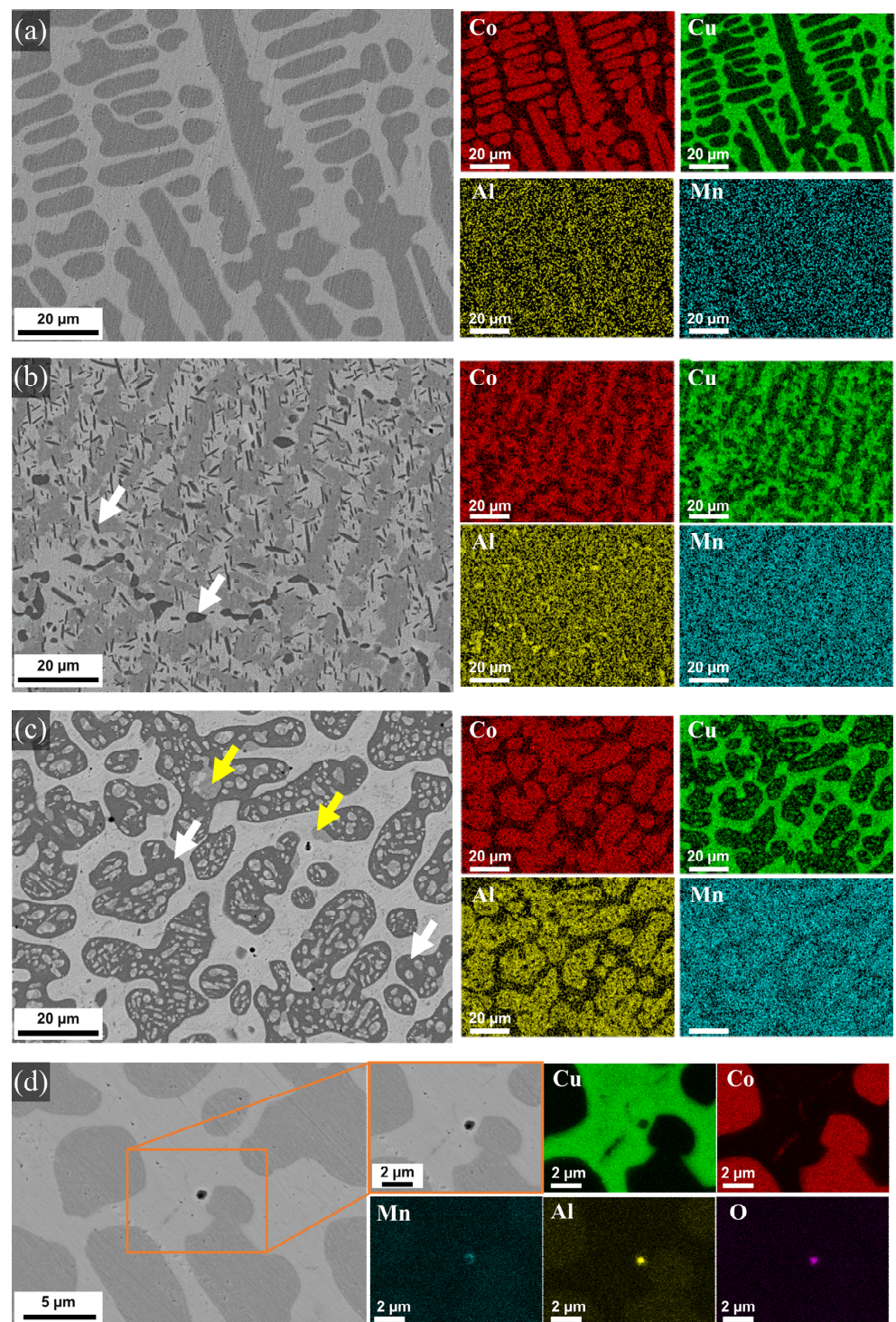


Figure 3. Back-scattered electron (BSE) images with energy dispersive spectroscopy (EDS) maps for Al, Co, Cu, and Mn of the (a) 2.5Al, (b) 10Al, and (c) 15Al alloys. The white and yellow arrows in (b,c) indicate B2 and Co-rich FCC, respectively. (d) High-magnification BSE images with EDS maps for Al, Co, Cu, Mn, and O in the 2.5Al alloys, indicating the AlMn-rich oxide.

Table 1. The averaged chemical compositions with standard deviations and configurational entropy of the dual FCC and B2 phases in the 2.5Al, 10Al, and 15Al alloys obtained by EDS.

Alloys	Phases	Chemical Composition, at%				ΔS_{mix}
		Al	Co	Cu	Mn	
2.5Al	Overall	2.95 ± 0.15	47.90 ± 0.50	46.30 ± 0.70	2.85 ± 0.05	-
	Co-rich FCC	2.85 ± 0.15	78.85 ± 4.55	15.50 ± 4.80	2.80 ± 0.10	0.68R
	Cu-rich FCC	1.55 ± 0.05	10.15 ± 0.25	86.05 ± 0.15	2.25 ± 0.05	0.51R
10Al	Overall	11.50 ± 0.40	39.60 ± 0.10	38.30 ± 0.20	10.55 ± 0.05	-
	Co-rich FCC	7.40 ± 0.10	64.50 ± 1.30	15.90 ± 1.60	12.20 ± 0.20	1.02R
	Cu-rich FCC	3.55 ± 0.05	10.20 ± 0.50	79.20 ± 0.50	7.05 ± 0.05	0.72R
	B2	26.95 ± 0.15	57.60 ± 0.10	2.55 ± 0.05	12.90 ± 0.20	1.03R
15Al	Overall	16.15 ± 2.05	35.05 ± 0.30	33.50 ± 2.50	15.30 ± 0.30	-
	Co-rich FCC	5.65 ± 0.15	63.90 ± 0.40	12.35 ± 0.65	18.10 ± 0.10	1.02R
	Cu-rich FCC	3.25 ± 0.25	13.00 ± 2.30	72.60 ± 1.80	11.15 ± 0.25	0.85R
	B2	23.85 ± 0.15	56.05 ± 0.05	3.25 ± 0.25	16.85 ± 0.35	1.08R

Table 2. The calculated fractions based on Thermo-Calc software and actual phase fraction of Co-rich FCC, Cu-rich FCC, and B2 in the present alloys.

Alloys	Phase Fractions	Co-Rich FCC, %	Cu-Rich FCC, %	B2, %
2.5Al	Calculated	50.27	49.73	-
	Actual	52.57 ± 1.15	47.43 ± 1.15	-
10Al	Calculated	39.64	40.85	19.51
	Actual	44.57 ± 0.26	40.10 ± 0.55	15.33 ± 0.47
15Al	Calculated	18.86	37.81	43.33
	Actual	17.47 ± 2.28	39.63 ± 1.36	42.90 ± 0.99

The inverse pole figure (IPF) and phase maps of the alloys are shown in Figure 4. The 2.5Al alloy shows dual FCC dendrites, which have highly coherent grain orientation relations because of the same solidification direction during cooling (Figure 4a,b). As the Al content increases, the 10Al and 15Al alloys show additional B2 phases with dual FCC domains (Figure 4c–f). The needle-shaped B2 phases are sprinkled in the 10Al alloy (Figure 4c,d), while the dendritic B2 phases exist in the 15Al alloy (Figure 4e,f). The length and width of the needle-shaped B2 precipitates in the 10Al alloy are $1.58 \pm 0.68 \mu\text{m}$ and $0.33 \pm 0.15 \mu\text{m}$, respectively, while the size of the dendritic B2 in the 15Al alloy is $10.40 \pm 3.81 \mu\text{m}$.

3.2. Mechanical Properties of the Al-Co-Cu-Mn IMMEAs

The tensile properties and strain hardening rates (SHRs) of the homogenized alloys are presented in Figure 5a–c. With the addition of Al and Mn, the YS and ultimate tensile strength (UTS) of the 2.5Al, 10Al, and 15Al alloys increases from 252.8 ± 9.8 and 437.7 ± 12.3 MPa (2.5Al) to 376.2 ± 25.7 and 610.6 ± 44.3 MPa (10Al), and 546.3 ± 19.0 and 760.8 ± 12.9 MPa (15Al), respectively. Simultaneously, the total elongation decreases from $65.9 \pm 7.9\%$ to $9.1 \pm 0.3\%$. The formation of B2 phases enhances YS and UTS; however, it deteriorates the elongation. The SHR of the alloys improves with the addition of Al and Mn (Figure 5c). Notably, the 15Al exhibits higher SHR compared to the 2.5Al and 10Al alloys.

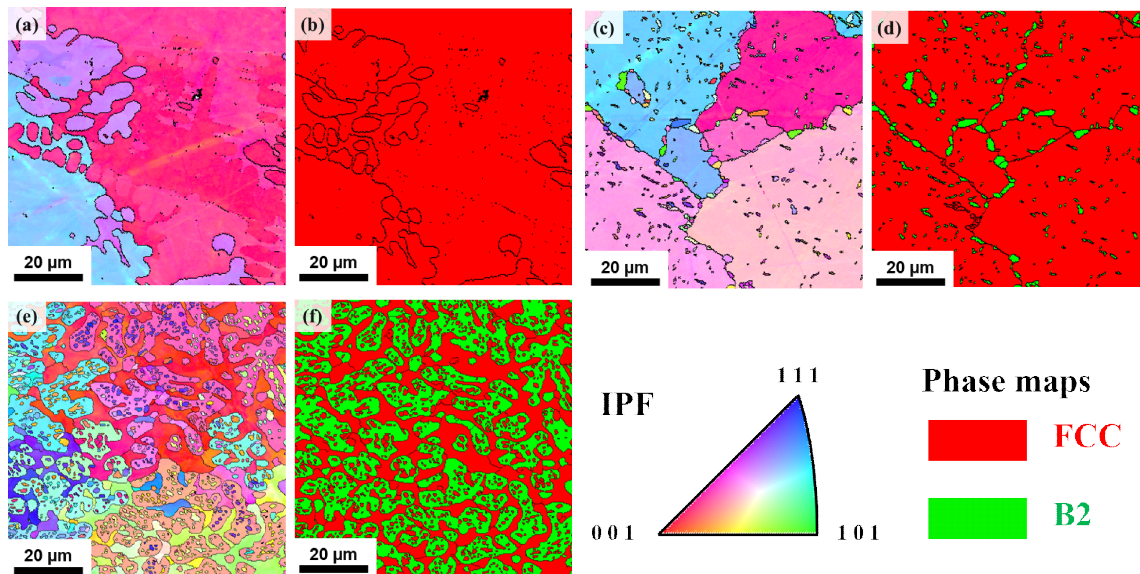


Figure 4. Inverse pole figure (IPF) and phase maps of (a,b) the 2.5Al, (c,d) 10Al, and (e,f) 15Al alloys.

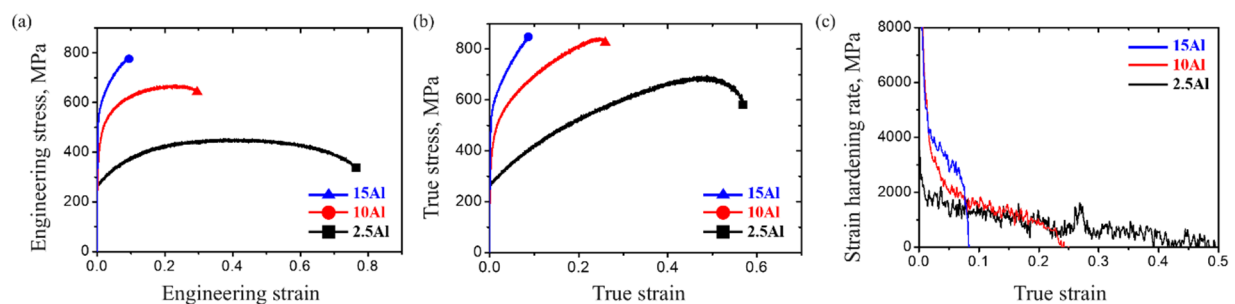


Figure 5. (a) Engineering and (b) true stress-strain curves of the present alloys. (c) Strain hardening rates (SHR) versus true strain of the present alloys.

To elucidate the difference in SHR values of the present alloys, the HDI stress was measured using the LUR test (Figure 6a). The HDI stress was calculated from the average stress of unloading yield stress and reloading yield stress, using the following equation [28]:

$$\sigma_{\text{HDI}} = \frac{\sigma_u + \sigma_r}{2} \quad (4)$$

where σ_{HDI} , σ_u , and σ_r are the HDI stress, unloading yield stress, and reloading yield stress, respectively. The unloading and reloading stress are defined as the points which have a 10% reduction in slope from effective elastic modulus. The effective stress can be determined as follows [28]:

$$\sigma_{\text{effective}} = \sigma_{\text{flow}} - \sigma_{\text{HDI}} \quad (5)$$

where $\sigma_{\text{effective}}$ and σ_{flow} are the effective stress and flow stress, respectively.

The measured effective and HDI stresses of the 2.5Al alloy are 125–250 MPa and 158–327 MPa, respectively (Figure 6b). With the increase in Al content, the HDI stress values of the alloys become higher. The HDI stress substantially enhances from 308–500 MPa in the 10Al alloy to 340–460 MPa in the 15Al alloy. The 2.5Al alloy maintains HDI stress similar to effective stress during deformation, while the 10Al and 15Al alloys show much higher HDI stress than their corresponding effective stress.

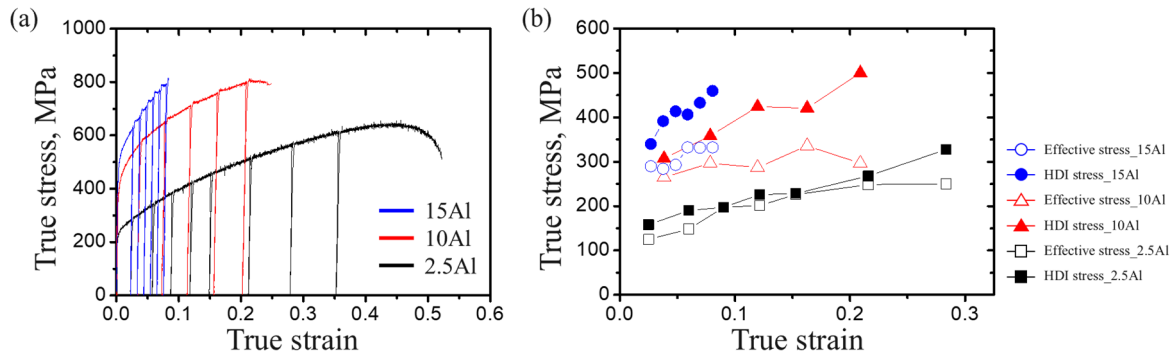


Figure 6. (a) Mechanical response during loading-unloading-reloading (LUR) cyclic deformation and (b) measured hetero-deformation induced (HDI) stress and effective stress of the present alloys.

3.3. Fractography

The fracture surface and the longitudinal section of the fractured samples are presented in Figure 7. It can be seen that the 2.5Al and 10Al alloys show ductile fractures. The fracture surfaces of the 2.5Al and 10Al alloys consist of numerous dimples resulted from the ductile rupture of dual FCC, as shown in Figure 7a,b. The dimple size and depth are much smaller in the 10Al alloy than in the 2.5Al alloy. In Figure 7c, the 15Al alloy shows a ductile fracture mode with a brittle fracture in the B2 phase. The magnified longitudinal sections of the fractured samples are shown in Figure 7d–f. Decohesion along the phase boundary is observed in the 2.5Al alloy (Figure 7d), while the brittle fracture modes of the B2 phases are observed in the 10Al and 15Al alloys (Figure 7e,f).

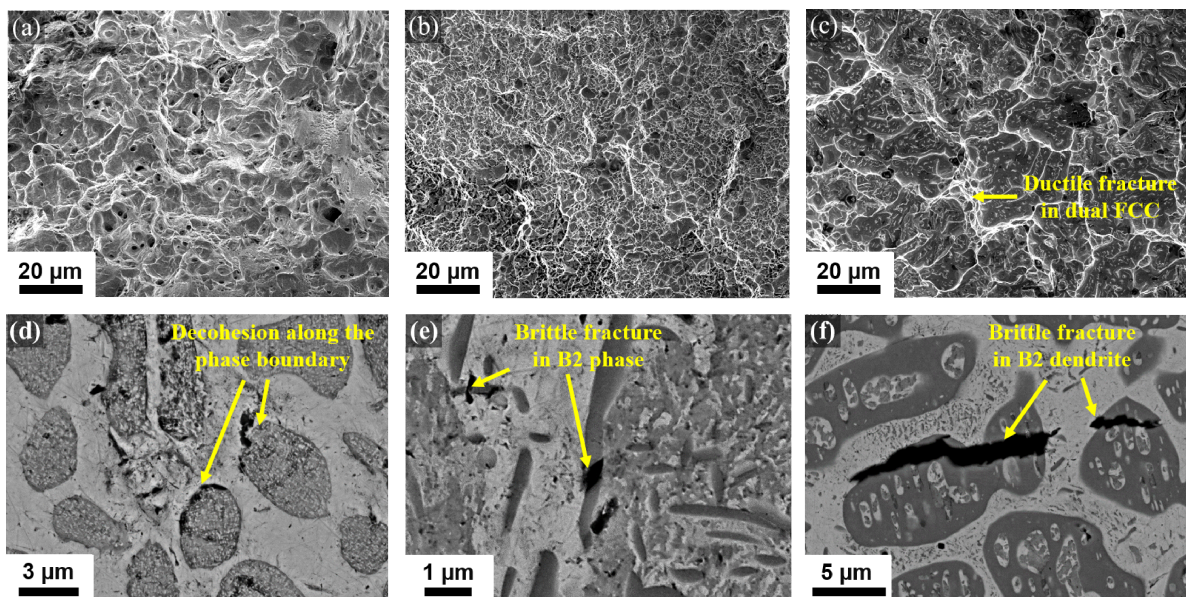


Figure 7. The (a–c) fracture surfaces and (d–f) longitudinal section of the (a,d) 2.5Al, (b,e) 10Al, and (c,f) 15Al alloys.

4. Discussion

The purpose of this study is to introduce a new IMMEA design using the immiscible nature of the Co-Cu binary system. We investigated the microstructural evolution and mechanical properties of the designed alloys. The binary Co-Cu alloy was expected to have dual FCC phases (Figure 1a). Therefore, an additional strengthening mechanism was applied to the Co-Cu-based IMMEA through the formation of the B2 phase by adding Al.

The thermodynamic calculation supports the formation of the B2 phase in the designed Al-Co-Cu-Mn system. From the microstructural analysis, the formation of the B2 phase

has been demonstrated in the 10Al and 15Al alloys (Figures 2–4). The B2 formation can be rationalized by the lattice distortion energy. Since the Al atom is larger than the other elements [37], Al addition stabilizes the BCC structure, which has a lower atomic packing density than the FCC structure [38]. Notably, the mixing enthalpy of the Co-Al pair is -19 kJ/mol, indicating that its ordering tendency is stronger than that of other combinations of pairs in the Al-Co-Cu-Mn system [39–41], resulting in the formation of an Al-Co-ordered B2 phase [38].

The hard B2 phases are absent in the 2.5Al alloy, while they are formed in the 10Al and 15Al alloys with considerable fractions of 14.75% and 42.90%, respectively (Figure 3 and Table 2). The shape and distribution of the B2 phases are totally different between the 10Al and 15Al alloys. The needle-shaped B2 phases are finely distributed in the 10Al alloy, while dendritic B2 phases are observed in the 15Al alloy. The solidification temperature of the B2 phase becomes higher as the Al and Mn contents in the alloys increase, according to the thermodynamic calculation (Figure 1c,d). In the 15Al alloy, the B2 phases are solidified at first during the casting process; thus, the B2 phases have a dendritic microstructure, and dual FCC are formed in the inter-dendritic microstructure. Meanwhile, the dual FCC phases in the 2.5Al and 10Al alloys also show dendritic and inter-dendritic microstructures. It should be noted that spherical morphologies are observed in the microstructure that underwent liquid-liquid phase separation [42]. However, the present Al-Co-Cu-Mn alloys exhibit typical dendritic and inter-dendritic microstructures, meaning that the resulting microstructure is not a footprint of the liquid-liquid phase separation during casting. It should also be noted that the spherical FCC precipitates are formed inside the B2 dendrites. The formation of FCC precipitates may be associated with the super-saturated solid solutions of Co and Cu in the B2 phase at high temperatures. During cooling to room temperature, the dual FCC phases are precipitated in B2 dendrites due to the decreased solubility with lowering temperature [26]. These FCC precipitates are coarsened to spherical precipitates during homogenization [43]. On the other hand, the B2 phase in the 10Al alloy exists as a precipitate in the FCC matrix because the temperature of the B2 formation is lower than that of the Co-rich FCC phase. The compositional segregation of Al and Mn in the Co-rich and Cu-rich phases can be elucidated by the relatively high mixing enthalpy of Al-Cu and Cu-Mn pairs compared to that of Al-Co and Co-Mn pairs [40]. It appears as the selective dissolution of Al and Mn in Co, which stabilizes the Cu-rich FCC instead of Cu-rich BCC/L2₁ observed in the Al-Cu-Fe-Mn IMMEDAs [26]. In addition, the needle-shaped B2 precipitates of the 10Al alloy are mostly formed in the Cu-rich region due to the high mixing enthalpy of Al-Cu and Co-Cu pairs. [40].

The representative strengthening mechanisms ($\Delta\sigma_y$) of the present alloys can be expressed by

$$\Delta\sigma_y = \Delta\sigma_{SS} + \Delta\sigma_{PPT} + \Delta\sigma_{HDI} \quad (6)$$

where $\Delta\sigma_{SS}$, $\Delta\sigma_{PPT}$, and $\Delta\sigma_{HDI}$ are the strengthening by solid solution, precipitation, and hetero-deformation, respectively. The solid solution strengthening of the present alloys is generated from lattice distortion caused by the larger Al atom [37,38]. Moreover, the hard B2 precipitates in the 10Al alloy contribute to the increased YS by precipitation strengthening. The precipitation strengthening ($\Delta\sigma_{PPT}$) induced by needle-shaped precipitates is calculated, as follows [44]:

$$\Delta\sigma_{PPT} = 2\beta GbM \left(\frac{f}{2\pi} \right)^{1/2} \frac{1}{r_m} \quad (7)$$

where β is the constant (0.5), G is the shear modulus (53 GPa), b is the Burgers vector (0.257 nm), M is the Taylor factor (3.06 for FCC), f is the fraction of precipitates (14.75%), and r_m is the mean radius of precipitates. In the 10Al alloy, the needle-shaped precipitates are assumed to be only on the Cu-rich domain, as observed in Figure 3b. The shear modulus of the Cu-rich phase in the 10Al alloy is determined by the rule of mixtures involving the constituent elements in Table 1 [45–47]. The lattice parameters of the Cu-rich phase in the

10Al (0.363 nm) and 15Al (0.365 nm) alloys were obtained from the XRD measurement in Figure 2. The Burgers vectors along the <110> direction of the Cu-rich FCC phase in the 10Al and 15Al alloys were calculated from the lattice parameters. The effective mean radius of a needle-shaped r_m is described by [48]:

$$r_m = \sqrt[3]{\frac{3\delta}{4\pi}}w, \quad (8)$$

$$\delta = \frac{l}{w}, \quad (9)$$

where l and w are the length (1.58 μm) and width (0.33 μm) of precipitates, respectively. Combining Equations (7) and (8), the $\Delta\sigma_{\text{PPT}}$ can be calculated to be ~ 19 MPa. Meanwhile, the B2 and Cu-rich FCC phases in the 15Al alloy are revealed as dendritic and interdendritic microstructures. If we assume the dendritic B2 precipitates as an equiaxed precipitate, the contribution of precipitation strengthening in the 15Al alloy is quantified, as follows [10]:

$$\Delta\sigma_{\text{PPT}} = M \frac{0.4Gb}{\pi\lambda} \frac{\ln\left(\frac{2r}{b}\right)}{\sqrt{1-\nu}}, \quad (10)$$

$$\lambda = 2r \left(\sqrt{\frac{\pi}{4f}} - 1 \right), \quad (11)$$

$$r = \frac{d}{2} \sqrt{\frac{2}{3}}, \quad (12)$$

where G and b are the shear modulus (55 GPa) and Burgers vector (0.258 nm) of Cu-rich FCC in the 15Al alloy, respectively. ν is the Poisson's ratio (assumed to be 0.3), f is the fraction of B2 precipitates (42.90%), and d is the grain size of the B2 phases (10.40 μm). From Equations (10)–(12), the $\Delta\sigma_{\text{PPT}}$ of the 15Al alloy is calculated as ~ 23 MPa. Hence, the conventional precipitation strengthening cannot describe the whole increments of yield strength in the 10Al and 15Al alloys. The additional strengthening mechanism of the 10Al and 15Al alloys is associated with the co-existing hard B2 and soft FCC domains, resulting in HDI strengthening ($\Delta\sigma_{\text{HDI}}$) [49,50]. In heterogeneous materials, the plastic strain is partitioned due to high plastic incompatibility between hard and soft domains [27]. To relieve and maintain the compatibility between domain boundaries, geometrically necessary dislocations (GNDs) are generated and piled up at the domain boundary, leading to HDI strengthening [27]. The B2/FCC interphase boundary in the 10Al and 15Al alloys contributes to the $\Delta\sigma_{\text{HDI}}$. Consequently, the YS, UTS, and strain hardening of the 10Al and 15Al alloys improve substantially compared to the 2.5Al alloy (Figure 5). It should also be noted that the highest HDI stress at the same true strain is achieved in the 15Al alloy (Figure 6b).

The ductility of the present alloys can be explained by the corresponding fracture mechanism. The elongation of the alloys decreases rapidly from the 2.5Al to 10Al and 15Al alloys. This stems from the changes of fracture mode from ductile fracture to ductile-brittle mixed fracture. The ordered B2 phase lacks a number of independent slip systems, leading to brittle fracture [51]. Therefore, unlike the ductile dual FCC-structured 2.5Al alloy, the brittle fracture is observed in the 10Al and 15Al alloys (Figure 7). Once the crack initiates in the B2 phase, the crack propagates within the B2 phase and then stops at the B2/FCC interphase boundary (Figure 7e,f). This process introduces profuse void nucleation at the interphase boundary; as a result, it may lead to earlier failure of the B2-containing 10Al and 15Al alloys than the 2.5Al alloy. Nevertheless, the 15Al alloy retains a reasonable elongation of 9% even with the high fraction of the B2 phase over 40%, due to the extra strain hardening through HDI strengthening.

5. Conclusions

In summary, the microstructural evolution and mechanical properties of the developed Al-Co-Cu-Mn IMMEAs were investigated. The 2.5Al alloy shows dual FCC phases generated by the immiscible nature of the Co-Cu binary system. As the contents of Al increase, the microstructure of the alloys transforms from dual FCC (Co-rich FCC and Cu-rich FCC) phases to triple phases (dual FCC and B2). The CoAl-rich B2 phase is found to have a needle-like shape or dendritic microstructure depending on the Al content. The contribution of yield strength in the 10Al and 15Al alloys cannot be explained through conventional precipitation strengthening. The hard B2 and soft Cu-rich FCC domains co-exist in the 10Al and 15Al alloys, leading to significant HDI strengthening of the alloys. The HDI strengthening enables the alloys to possess excellent yield strength, ultimate tensile strength, and strain hardening rate while maintaining considerable ductility. The design strategy for improved strength with substantial strain hardening can be accomplished through the present design of heterogeneous IMMEAs.

Author Contributions: Conceptualization, S.S. and J.M.; methodology, S.S. and J.M.; software, P.A.R.; validation, S.S., J.M. and H.S.K.; formal analysis, S.S., J.M. and H.K. (Hyeonseok Kwon); investigation, S.S. and H.K. (Hyeonseok Kwon); resources, H.S.K.; data curation, S.S., J.M. and H.K. (Hyeonseok Kwon); writing—original draft preparation, S.S.; writing—review and editing, J.M. and H.S.K.; visualization, S.S.; supervision, H.S.K. and H.K. (Hidemi Kato); project administration, H.S.K.; funding acquisition, H.S.K. All authors have read and agreed to the published version of the manuscript.

Funding: This research was supported by Creative Materials Discovery Program through the National Research Foundation of Korea (NRF) funded by the Ministry of Science and ICT (2016M3D1A1023384). JM acknowledges the support from Basic Science Research Program through the National Research Foundation of Korea (NRF) funded by the Ministry of Education [2020R1A6A3 A03037509].

Institutional Review Board Statement: Not applicable.

Informed Consent Statement: Not applicable.

Conflicts of Interest: The authors declare no conflict of interest.

References

1. Yeh, J.-W.; Chen, S.-K.; Lin, S.-J.; Gan, J.-Y.; Chin, T.-S.; Shun, T.-T.; Tsau, C.-H.; Chang, S.-Y. Nanostructured High-Entropy Alloys with Multiple Principal Elements: Novel Alloy Design Concepts and Outcomes. *Adv. Eng. Mater.* **2004**, *6*, 299–303. [\[CrossRef\]](#)
2. Zhang, Y.; Gao, M.C.; Yeh, J.W.; Liaw, P.K. *Overview of High-Entropy Alloys: Fundamentals and Applications*; Springer International Publishing: Cham, Switzerland, 2016; pp. 1–12.
3. Yeh, J.-W. Recent Progress in High-entropy Alloys. *Ann. Chim. Sci. Mat.* **2006**, *31*, 633–648. [\[CrossRef\]](#)
4. Cantor, B.; Chang, I.T.H.; Knight, P.; Vincent, A.J.B. Microstructural development in equiatomic multicomponent alloys. *Mater. Sci. Eng. A* **2004**, *375–377*, 213–218. [\[CrossRef\]](#)
5. Sohn, S.S.; Da Silva, A.K.; Ikeda, Y.; Kormann, F.; Lu, W.; Choi, W.S.; Gault, B.; Ponge, D.; Neugebauer, J.; Raabe, D. Ultrastrong Medium-Entropy Single-Phase Alloys Designed via Severe Lattice Distortion. *Adv. Mater.* **2018**, *31*, 1807142. [\[CrossRef\]](#)
6. Gludovatz, B.; Hohenwarter, A.; Catoor, D.; Chang, E.H.; George, E.P.; Ritchie, R.O. A fracture-resistant high-entropy alloy for cryogenic applications. *Science* **2014**, *345*, 1153–1158. [\[CrossRef\]](#)
7. Kumar, N.A.P.K.; Li, C.; Leonard, K.J.; Bei, H.; Zinkle, S.J. Microstructural stability and mechanical behavior of FeNiMnCr high entropy alloy under ion irradiation. *Acta Mater.* **2016**, *113*, 230–244. [\[CrossRef\]](#)
8. Bae, J.W.; Seol, J.B.; Moon, J.; Sohn, S.S.; Jang, M.J.; Um, H.Y.; Lee, B.-J.; Kim, H.S. Exceptional phase-transformation strengthening of ferrous medium-entropy alloys at cryogenic temperatures. *Acta Mater.* **2018**, *161*, 388–399. [\[CrossRef\]](#)
9. Bae, J.W.; Park, J.M.; Moon, J.; Choi, W.M.; Lee, B.-J.; Kim, H.S. Effect of μ -precipitates on the microstructure and mechanical properties of non-equiatomic CoCrFeNiMo medium-entropy alloys. *J. Alloys Compd.* **2019**, *781*, 75–83. [\[CrossRef\]](#)
10. Kwon, H.; Moon, J.; Bae, J.W.; Park, J.M.; Son, S.; Do, H.-S.; Lee, B.-J.; Kim, H.S. Precipitation-driven metastability engineering of carbon-doped CoCrFeNiMo medium-entropy alloys at cryogenic temperature. *Scr. Mater.* **2020**, *188*, 140–145. [\[CrossRef\]](#)
11. He, J.Y.; Wang, H.; Huang, H.L.; Xu, X.D.; Chen, M.W.; Wu, Y.; Liu, X.J.; Nieh, T.G.; An, K.; Lu, Z.P. A precipitation-hardened high-entropy alloy with outstanding tensile properties. *Acta Mater.* **2016**, *102*, 187–196. [\[CrossRef\]](#)
12. Li, Z.; Tasan, C.C.; Springer, H.; Gault, B.; Raabe, D. Interstitial atoms enable joint twinning and transformation induced plasticity in strong and ductile high-entropy alloys. *Sci. Rep.* **2017**, *7*, 40704. [\[CrossRef\]](#) [\[PubMed\]](#)

13. Yang, H.; Li, J.; Guo, T.; Wang, W.Y.; Kou, H.; Wang, J. Fully Recrystallized Al_{0.5}CoCrFeNi High-Entropy Alloy Strengthened by Nanoscale Precipitates. *Met. Mater. Int.* **2019**, *25*, 1145–1150. [[CrossRef](#)]
14. Rogal, L.; Szklarz, Z.; Bobrowski, P.; Kalita, D.; Garzel, G.; Tarasek, A.; Kot, M.; Szlezzynger, M. Microstructure and Mechanical Properties of Al–Co–Cr–Fe–Ni Base High Entropy Alloys Obtained Using Powder Metallurgy. *Met. Mater. Int.* **2019**, *25*, 930–945. [[CrossRef](#)]
15. Li, Z.; Pradeep, K.G.; Deng, Y.; Raabe, D.; Tasan, C.C. Metastable high-entropy dual-phase alloys overcome the strength–ductility trade-off. *Nature* **2016**, *534*, 227–230. [[CrossRef](#)]
16. Kim, D.G.; Jo, Y.H.; Yang, J.; Choi, W.-M.; Kim, H.S.; Lee, B.-J.; Sohn, S.S.; Lee, S. Ultrastrong duplex high-entropy alloy with 2 GPa cryogenic strength enabled by an accelerated martensitic transformation. *Scr. Mater.* **2019**, *171*, 67–72. [[CrossRef](#)]
17. Lu, Y.; Dong, Y.; Guo, S.; Jiang, L.; Kang, H.; Wang, T.; Wen, B.; Wang, Z.; Jie, J.; Cao, Z.; et al. A Promising New Class of High-Temperature Alloys: Eutectic High-Entropy Alloys. *Sci. Rep.* **2014**, *4*, 6200. [[CrossRef](#)]
18. Shi, P.; Ren, W.; Zheng, T.; Ren, Z.; Hou, X.; Peng, J.; Hu, P.; Gao, Y.; Zhong, Y.; Liaw, P.K. Enhanced strength–ductility synergy in ultrafine-grained eutectic high-entropy alloys by inheriting microstructural lamellae. *Nat. Commun.* **2019**, *10*, 489. [[CrossRef](#)]
19. Gao, X.; Lu, Y.; Zhang, B.; Liang, N.; Wu, G.; Sha, G.; Liu, J.; Zhao, Y. Microstructural origins of high strength and high ductility in an AlCoCrFeNi_{2.1} eutectic high-entropy alloy. *Acta Mater.* **2017**, *141*, 59–66. [[CrossRef](#)]
20. Gasan, H.; Ozcan, A. New Eutectic High-Entropy Alloys Based on Co–Cr–Fe–Mo–Ni–Al: Design, Characterization and Mechanical Properties. *Met. Mater. Int.* **2020**, *26*, 1152–1167. [[CrossRef](#)]
21. Chen, X.; Gao, D.; Hu, J.X.; Liu, Y.; Tang, C.P. Evolution of Microstructures and Properties in Al_xCrFeMn_{0.8}Ni_{2.1} HEAs. *Met. Mater. Int.* **2020**, *25*, 1135–1144. [[CrossRef](#)]
22. Dobbstein, H.; Gurevich, E.L.; George, E.P.; Ostendorf, A.; Laplanche, G. Laser metal deposition of compositionally graded TiZrNbTa refractory high-entropy alloys using elemental powder blends. *Addit. Manuf.* **2019**, *25*, 252–262. [[CrossRef](#)]
23. Gwalani, B.; Soni, V.; Waseem, O.A.; Mantri, S.A.; Banerjee, R. Laser additive manufacturing of compositionally graded AlCrFeMoV_x (x=0 to 1) high-entropy alloy system. *Opt. Laser Technol.* **2019**, *113*, 330–337. [[CrossRef](#)]
24. Song, M.; Zhou, R.; Gu, J.; Wang, Z.; Ni, S.; Liu, Y. Nitrogen induced heterogeneous structures overcome strength-ductility trade-off in an additively manufactured high-entropy alloy. *Appl. Mater. Today* **2020**, *18*, 100498. [[CrossRef](#)]
25. Jiang, F.; Zhao, C.; Liang, D.; Zhu, W.; Zhang, Y.; Pan, S.; Ren, F. In-situ formed heterogeneous grain structure in spark-plasma-sintered CoCrFeMnNi high-entropy alloy overcomes the strength-ductility trade-off. *Mater. Sci. Eng. A* **2020**, *771*, 138625. [[CrossRef](#)]
26. Moon, J.; Park, J.M.; Bae, J.W.; Do, H.-S.; Lee, B.-J.; Kim, H.S. A new strategy for designing immiscible medium-entropy alloys with excellent tensile properties. *Acta Mater.* **2020**, *193*, 71–82. [[CrossRef](#)]
27. Zhu, Y.; Wu, X. Perspective on hetero-deformation induced (HDI) hardening and back stress. *Mater. Res. Lett.* **2019**, *7*, 393–398. [[CrossRef](#)]
28. Yang, M.; Pan, Y.; Yuan, F.; Zhu, Y.; Wu, X. Back stress strengthening and strain hardening in gradient structure. *Mater. Res. Lett.* **2016**, *4*, 145–151. [[CrossRef](#)]
29. Kim, J.G.; Jang, M.J.; Park, H.K.; Chin, K.-G.; Lee, S.; Kim, H.S. Back-Stress Effect on the Mechanical Strength of TWIP-IF Steels Layered Sheet. *Met. Mater. Int.* **2019**, *25*, 912–917. [[CrossRef](#)]
30. Zhao, J.-Z.; Ahmed, T.; Jiang, H.-X.; He, J.; Sun, Q. Solidification of Immiscible Alloys: A Review. *Acta Metall. Sin.* **2017**, *30*, 1–28. [[CrossRef](#)]
31. Sundman, B.; Jansson, B.; Andersson, J.-O. The Thermo-Calc databank system. *Calphad* **1985**, *9*, 153–190. [[CrossRef](#)]
32. KTH. Upgraded by TCFE2000. In *The Thermo-Calc Steels Database*; Lee, B.-J., Sundman, B., Eds.; KTH: Stockholm, Sweden, 1999.
33. Chin, K.-G.; Lee, H.-J.; Kwak, J.-H.; Kang, J.-Y.; Lee, B.-J. Thermodynamic calculation on the stability of (Fe,Mn)₃AlC carbide in high aluminum steels. *J. Alloys Compd.* **2010**, *505*, 217–223. [[CrossRef](#)]
34. Stein, F.; He, C.; Dupin, N. Melting behaviour and homogeneity range of B2 CoAl and updated thermodynamic description of the AlCo system. *Intermetallics* **2013**, *39*, 58–68. [[CrossRef](#)]
35. Liu, X.J.; Ohnuma, I.; Kainuma, R.; Ishida, K. Phase equilibria in the Cu-rich portion of the Cu–Al binary system. *J. Alloys Compd.* **1998**, *264*, 201–208. [[CrossRef](#)]
36. Wang, C.P.; Liu, X.J.; Ohnuma, I.; Kainuma, R.; Ishida, K. Thermodynamic assessments of the Cu–Mn–X (X: Fe, Co) systems. *J. Alloys Compd.* **2007**, *438*, 129–141. [[CrossRef](#)]
37. Egami, T.; Waseda, Y. Atomic size effect on the formability of metallic glasses. *J. Non-Cryst. Solids* **1984**, *64*, 113–134. [[CrossRef](#)]
38. He, J.Y.; Liu, W.H.; Wang, H.; Wu, Y.; Liu, X.J.; Nieh, T.G.; Lu, Z.P. Effects of Al addition on structural evolution and tensile properties of the FeCoNiCrMn high-entropy alloy system. *Acta Mater.* **2014**, *62*, 105–113. [[CrossRef](#)]
39. Praveen, S.; Murty, B.S.; Kottada, R.S. Alloying behavior in multi-component AlCoCrCuFe and NiCoCrCuFe high entropy alloys. *Mater. Sci. Eng. A* **2012**, *534*, 83–89. [[CrossRef](#)]
40. Wu, C.-S.; Tsai, P.-H.; Kuo, C.-M.; Tsai, C.-W. Effect of Atomic Size Difference on the Microstructure and Mechanical Properties of High-Entropy Alloys. *Entropy* **2018**, *20*, 967. [[CrossRef](#)]
41. Jiang, C.; Chen, L.-Q.; Kiu, Z.-K. First-principles study of constitutional point defects in B2 NiAl using special quasirandom structures. *Acta Mater.* **2005**, *53*, 2643–2652. [[CrossRef](#)]
42. Liu, S.; Jie, J.; Dong, B.; Guo, Z.; Wang, T.; Li, T. Novel insight into evolution mechanism of second liquid-liquid phase separation in metastable immiscible Cu-Fe alloy. *Mater. Des.* **2018**, *156*, 71–81. [[CrossRef](#)]

43. Yu, Y.; Shi, P.; Feng, K.; Liu, J.; Cheng, J.; Qiao, Z.; Yang, J.; Li, J.; Liu, W. Effects of Ti and Cu on the Microstructure Evolution of AlCoCrFeNi High-Entropy Alloy During Heat Treatment. *Acta Metall. Sin.* **2020**, *33*, 1077–1090. [[CrossRef](#)]
44. Bahrami, A.; Miroux, A.; Sietsma, J. An Age-Hardening Model for Al-Mg-Si Alloys Considering Needle-Shaped Precipitates. *Metall. Mater. Trans. A* **2012**, *43*, 4445–4453. [[CrossRef](#)]
45. Edalati, K.; Horita, Z. High-pressure torsion of pure metals: Influence of atomic bond parameters and stacking fault energy on grain size and correlation with hardness. *Acta Mater.* **2011**, *59*, 6831–6836. [[CrossRef](#)]
46. Kaloyeros, A.E.; Pan, Y.; Goff, J.; Arkles, B. Review—Cobalt Thin Films: Trends in Processing Technologies and Emerging Applications. *ECS J. Solid State Sci. Technol.* **2019**, *8*, 119–152. [[CrossRef](#)]
47. AZO Materials. Available online: <https://www.azom.com/article.aspx?ArticleID=9102> (accessed on 29 December 2020).
48. Holmedal, B.; Osmundsen, E.; Du, Q. Precipitation of Non-Spherical Particles in Aluminum Alloys Part I: Generalization of the Kampmann–Wagner Numerical Model. *Metall. Mater. Trans. A* **2016**, *47*, 581–588. [[CrossRef](#)]
49. Jin, X.; Bi, J.; Zhang, L.; Zhou, Y.; Du, X.; Liang, Y.; Li, B. A new CrFeNi₂Al eutectic high entropy alloy system with excellent mechanical properties. *J. Alloys Compd.* **2019**, *770*, 655–661. [[CrossRef](#)]
50. Jin, X.; Zhou, Y.; Zhang, L.; Du, X.; Li, B. A new pseudo binary strategy to design eutectic high entropy alloys using mixing enthalpy and valence electron concentration. *Mater. Des.* **2018**, *143*, 49–55. [[CrossRef](#)]
51. Kimura, Y.; Kuriyama, H.; Suzuki, T.; Mishima, Y. Microstructure Control and Mechanical Properties of Binary Co-Al Alloys Based on B2 Intermetallic Compound CoAl. *Mater. Trans. JIM* **1994**, *35*, 182–188. [[CrossRef](#)]